中国光学（中英文） Chinese Optics 核心期刊

Research on the hyperspectral detection of greenhouse gas using Fabry-Perot interferometric system

LU Chuang, LI Zong-xuan, LI Lin, GU Zhi-yuan, TAO Shu-ping, YU Jiang-tao, NING Jiu-xin

Citation:
LU Chuang, LI Zong-xuan, LI Lin, GU Zhi-yuan, TAO Shu-ping, YU Jiang-tao, NING Jiu-xin. Research on the hyperspectral detection of greenhouse gas using Fabry–Perot interferometric system[J]. *Chinese Optics*, In press. doi: 10.37188/CO.EN–2025–0009
禄创, 李宗轩, 李林, 顾志远, 陶淑苹, 禹江涛, 宁久鑫. 基于法布里–珀罗干涉系统的温室气体高光谱探测研究[J]. 中国光学, 优先发表. doi: 10.37188/CO.EN–2025–0009

View online: https://doi.org/10.37188/CO.EN–2025–0009

中国光学（中英文）
Chinese Optics

文章编号　2097-1842(xxxx)x-0001-20

Research on the hyperspectral detection of greenhouse gas using Fabry-Perot interferometric system

LU Chuang[1,2,3], LI Zong-xuan[1,2,3 *], LI Lin[4 *], GU Zhi-yuan[1,2,3], TAO Shu-ping[1,2,3],
YU Jiang-tao[1,2,3], NING Jiu-xin[1,2,3]
（1. *Changchun Institute of Optics*, *Fine Mechanics and Physics*, *Chinese Academy of Sciences*,
Changchun 130033, *China*;
2. *University of Chinese Academy of Sciences*, *Beijing* 100049, *China*;
3. *Key Laboratory of Space-Based Dynamic Fast Optical Imaging Technology*, *Chinese Academy of Sciences*,
Changchun 130033, *China*;
4. *Beijing Institute of Control Engineering*, *Beijing*, 100190）
* *Corresponding author*, *E-mail*: *lizongxuan@ciomp.ac.cn*; *cast_lilin@163.com*

Abstract: To accurately monitor methane emissions from point sources, this paper explores the use of a Fabry-Perot (F-P) interferometer as the spectroscopic element of a spatial imaging spectrometer, aiming to achieve both high spatial and high spectral resolution. The study focuses on constructing both theoretical and physical models of the F-P cavity to meet the technical requirements of methane point-source monitoring. First, an initial theoretical model of F-P cavity interference under ideal conditions is developed based on multi-beam interference theory. Building upon this, a corresponding geometric model is established by considering the effect of finite throughput aperture, from which a theoretical model under finite aperture conditions is derived. In addition, a more comprehensive theoretical framework is constructed by incorporating surface defect distribution functions to account for microscopic random inhomogeneities and curvature defects. In the physical model development, the F-P cavity is initially designed based on the ideal theoretical model to match the spectral characteristics of methane absorption. Using the finite-aperture theoretical model, the transmission intensity curve and its slope are analyzed, and the aperture size is precisely determined bases on the physical meaning of the slope. Subsequently, the physical model is further optimized by adjusting the wedge angle at the rear surface of the mirror. To meet specific spectral and technical targets, the allowable variation in the gap spacing between the two parallel mirrors is thoroughly analyzed, thereby defining the tolerance range for the cavity gap. Surface roughness, figure accuracy, and parallelism of the reflective surfaces are then specified according to surface defect considerations. Ultimately, the optimized F-P cavity achieves a spectral resolution of 0.29 nm, meeting the technical requirements for methane point-source monitoring. By

---

收稿日期:2025-02-19; **修订日期:**xxxx-xx-xx
基金项目:中文基金
Supported by the National Natural Science Foundation of China (No. 12472350, No. 52275083); the Youth Innovation Promotion Association of the Chinese Academy of Sciences (No. 2021218); the "Rising Light" Talent Program (No. E1X011Y6X0)

constructing a comprehensive theoretical model and optimizing the physical design, this study enables the realization of both high spectral and spatial resolution, provides a theoretical foundation for applying F-P interferometers in spatial imaging spectrometry, and supports the advancement of high-precision spectral detection technologies.

Key words: Fabry-Perot interferometer; methane monitoring; hyperspectral; multibeam interference; spectral resolution

基于法布里-珀罗干涉系统的温室气体高光谱探测研究

禄　创[1,2,3], 李宗轩[1,2,3 *], 李　林[4 *], 顾志远[1,2,3], 陶淑苹[1,2,3], 禹江涛[1,2,3], 宁久鑫[1,2,3]
（1. 长春光学精密机械与物理研究所 中国科学院, 吉林 长春 130033;
2. 中国科学院大学, 北京 100049;
3. 天基动态快速光学成像技术重点实验室 中国科学院, 吉林 长春 130033;
4. 北京控制工程研究所, 北京 100190）

摘要: 为了能够精确监测甲烷点源排放情况, 本文研究了将法布里-珀罗(F-P)干涉仪用作空间成像光谱仪的分光元件, 以实现高空间分辨率与高光谱分辨率的兼顾。围绕 F-P 腔的理论与物理模型构建展开研究, 旨在实现高光谱分辨率, 以满足甲烷排放点源监测的技术需求。首先, 基于多光束干涉理论, 构建了理想条件下的 F-P 腔干涉初始理论模型。在此基础上, 考虑有限通光孔径效应, 建立了相应的几何模型, 并推导出有限通光孔径条件下的 F-P 腔理论模型。此外, 通过引入表面缺陷分布函数, 进一步构建了包含微观随机不均匀性缺陷和曲率缺陷的 F-P 腔理论模型, 从而形成更完整的理论框架。在物理模型构建方面, 根据初始理论模型, 对 F-P 腔进行初步设计, 使其匹配甲烷吸收光谱的监测需求。基于有限通光孔径 F-P 腔的理论模型, 结合透射光强函数曲线及其斜率曲线, 精确确定 F-P 腔的通光孔径尺寸。在此基础上, 结合镜体背面楔角, 对 F-P 腔物理模型进行了进一步优化。接着, 以实现目标频谱特性和技术要求为导向, 深入分析 F-P 腔两平行平板间隙间距的允许变动范围, 从而确定了 F-P 腔间隙距离的公差范围。根据表面缺陷条件, 设计 F-P 腔反射表面的表面粗糙度、面形精度及平行度。最终, 优化后的 F-P 腔光谱分辨率达到 0.29 nm, 满足甲烷排放点源监测的技术要求。本研究通过构建更完整的 F-P 腔理论模型, 并优化其物理设计, 实现了高光谱分辨率和高空间分辨率的兼顾, 为 F-P 干涉仪在空间成像光谱仪中的应用奠定了理论基础, 同时为高精度光谱探测技术的发展提供了重要支撑。

关　键　词: 法布里-珀罗干涉仪; 甲烷监测; 高光谱; 多光束干涉; 光谱分辨率
中图分类号: TP394.1;TH691.9　**文献标志码:** A　**doi:** 10.37188/CO.EN-2025-0009　**CSTR:** 32171.14.CO.EN-2025-0009

1 Introduction

Methane emissions from the energy sector represent one of the largest sources of global methane release. At the same time, this sector also holds the greatest potential for emission reductions[1]. These emissions are predominantly concentrated in point sources, where a relatively small number of sources account for a disproportionately large share of total emissions[2]. To improve methane monitoring in the energy sector, it is essential to better observe methane plumes from industrial facilities, which requires satellite observations with higher spatial resolution. In addition, to accurately detect methane column concentrations, the spectral resolution of onboard imaging spectrometers must reach 0.3 nm or better[3].

Global monitoring satellites such as Sentinel-5P/TROPOMI[4], GOSat[5], GF-5/GMI[6], along with regional satellites like MethaneSAT, enable large-scale methane monitoring. However, these systems typically have low spatial resolution, resulting in significant dilution of plume peak concentrations and an inability to detect small emissions that collectively contribute a large portion of total emissions. GHGSat[7], a representative satellite for point-source detection, demonstrates excellent capabilities in monitoring and quantifying emissions from individual sources. However, as a commercial platform, the cost of data acquisition is high. Moreover, although hyperspectral instruments such as PRISMA[8] (Italy), EnMAP[9] (Germany), and AHSI onboard China's GF-5[10] and ZY-1 02D[11] satellites have demonstrated the capability to monitor methane point sources in the broad 2.3 μm absorption band, they are limited by relatively low spectral resolution. As a result, they are only effective in detecting methane concentration enhancements from super-emitters. Furthermore, the use of grating-based spectrometers in systems like AHSI leads to a complex optical and structural design, contributing to increased overall system weight.

Tab. 1 Methane monitoring satellites and some of their parametric indicators

Satellite	Sensor	Swath width/km	Spatial Resolution/km	Spectral Resolution /nm	Spectral Methods
Sentinel-5P	TROPOMI	2600	7	0.23	PG dispersion with reflection grating
GOSAT	TANSO-FTS	790	10.5	0.07	Michelson interferometer
FY-3D	GAS	1200	10	0.3	Michelson interferometer
GF-5	GMI	865	10.3	0.074	Spatial heterodyne spectroscopy
MethaneSAT	PILSM	200	0.1×0.4	0.25	Diffraction grating
GHGSat-D	WAF-P	12	0.05	0.3	F-P Interferometer
GHGSat-CX			0.03		
GF-5	AHSI	60	0.03	10	Convex grating Offner spectrometer
ZY-1-02D	AHSI	60	0.03	20	Convex grating Offner spectrometer
PRISMA	HYC	30	0.03	12	Prism
EnMAP	HSI	30	0.03	10	Curved prism

Since its invention in 1899, the Fabry-Perot (F-P) interferometer has been instrumental in precision metrology, laser resonators, and fiber-optic sensing applications[12]. It consists of two parallel, highly reflective mirrors, enabling multibeam interference within the cavity. The resulting interference transmission function is described by the Airy function, with high-order interference peaks achieving picometer-level linewidths, ideal for high-resolution spectroscopy. In recent years, F-P interferometers have been widely applied in high-precision gas detection. For instance, NASA's FPICC system employs an F-P etalon for precise spectral channel selection in CO_2 and O_2 measurements[13], while Vargas-Rodriguez et al. developed a MEMS-based tunable F-P sensor for CH_4 and CO detection[14-15]. F-P interferometers have also been integrated with photoacoustic spectroscopy for in-situ gases monitoring[16-17]. In volcanic studies, they improve SO_2 imaging by mitigating aerosol interference through spectral channel tuning[18]. Yinsheng Lv et al. initially used a low-precision F-P etalon for angle-resolved quantitative SO_2 measurements, In volcanic studies, they improve SO_2 imaging by mitigating aerosol interference through spectral channel tuning[19]. Notably, the GHGSat satellite employs a compact, fixed-cavity F-P imaging spectrometer to detect industrial-scale CH_4 emissions from space via short-wave infrared solar backscatter[20]. This marks the first successful application of an F-P interferometric imaging spectrometer for space-to-ground gas detection. In summary, the F-P interferometer demonstrates outstanding spectral resolution in various high-precision gas detection scenarios, owing to its narrowband multibeam interference characteristics.

To enable more precise monitoring of methane emissions from industrial point sources, this study proposes the use of an F-P cavity as a dispersive element in a spaceborne imaging spectrometer. As a core component of the spectrometer, the dispersion mechanism significantly influences the overall performance of the instrument[21]. Its parallel substrate design introduces minimal optical aberrations, allowing for simplified optics with preserved spatial resolution. Thanks to its high finesse and throughput, the F-P cavity enables high spectral resolution via interferometric dispersion. The integration of an F-P cavity allows the instrument to simultaneously achieve high spatial and spectral resolution[22], while its compact structure facilitates lightweight, efficient system integration. The spectrometer's optical system includes a telescope, imaging mirrors, and a spectroscopic module as shown in Fig. 1. This paper focuses on exploring the application of the F-P cavity in spaceborne imaging spectrometers for methane monitoring, with particular emphasis on its function as a dispersive component in spectral detection.

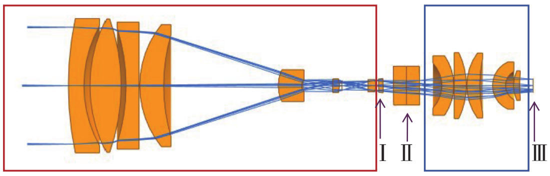

Fig. 1 Optical system of the space imaging spectrometer with F-P interferometric cavity. The red frame is the telescope group, the blue frame is the imaging mirror group; Ⅰ: filter, Ⅱ: F-P interference cavity, Ⅲ: focal plane

2 Mathematical modeling of F-P cavities

2.1 Multibeam interference theory

The F-P cavity typically consists of two parallel glass plates separated by a fixed distance. When monochromatic light enters the cavity at an angle θ relative to the normal, it undergoes multiple reflections and transmissions between the two mirrors, resulting in multi-beam interference. Upon reaching the mirror surfaces, part of the incident light is reflected while the rest is transmitted, as shown in Fig. 2. The phase difference between two adjacent rays (e.g., A and B, a and b) can be described as follows:

$$\varphi = 4\pi\mu d\sigma\cos\theta \quad , \tag{1}$$

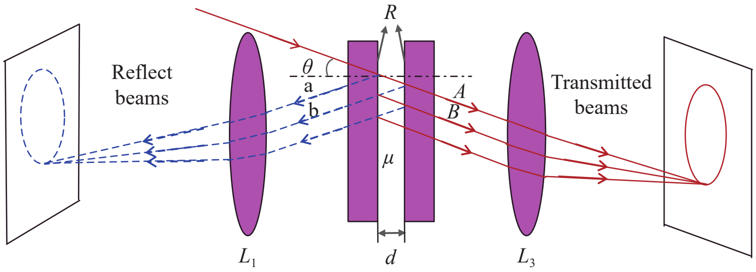

Fig. 2 Multiple beam interference in F-P cavity

where μ is the refractive index of the interstitial medium, d is the inter-mirror spacing, and σ is the wave number, defined as the reciprocal of the wavelength, i.e., $\sigma=\lambda^{-1}$. Based on the phase difference, the intensities of the reflected and transmitted light can be expressed as:

$$Y_r(\delta) = A_r(\delta)A_r^*(\delta) = R\left[1-2(R+\tau)\cos\delta+(R+\tau)^2\right]\left[1+R^2-2R\cos\delta\right]^{-1} , \tag{2}$$

$$Y_t(\delta) = A_t(\delta)A_t^*(\delta) = \tau^2\left[1+R^2-2R\cos\delta\right]^{-1} , \tag{3}$$

Here, R is the reflectivity of the mirror surface in the F-P cavity, and $\delta=\varphi+2\chi$, where χ denotes the phase change upon reflection at each surface. The above expressions can also be rewritten as

$$Y_r(\delta) = R\left[1+(1-A)^2-2(1-A)\cos\delta\right]\left(1+R^2-2R\cos\delta\right)^{-1} \quad , \tag{4}$$

$$Y_t(\delta)=\left[1-A(1-R)^{-1}\right]^2(1-R)^2\left(1+R^2-2R\cos\delta\right)^{-1}, \tag{5}$$

where A is the absorption/scattering coefficient, with the relation $R + \tau + A = 1$. Eq. (3.b) can also be represented using its equivalent forms:

$$Y_t(\delta) = \left[1-A(1-R)^{-1}\right]^2(1-R)(1+R)^{-1}\left[1+2\sum_{m=1}^{m=\infty}R^m\cos(m\delta)\right] \quad , \tag{6}$$

$$Y_t(\delta)=\left[1-A(1-R)^{-1}\right]^2\left[1+4R(1-R)^{-2}\sin^2\left(\frac{\delta}{2}\right)\right]^{-1}, \tag{7}$$

In general, the reflection mirrors of the F-P cavity are typically coated with multilayer dielectric films to ensure high reflectivity. The absorption and scattering losses introduced by these coatings are negligible; thus, the absorption/scattering coefficient A is considered to be zero in this study. When $A = 0$, the sum of Eq. (2.b) and Eq. (3.b), as well as their equivalent forms, equals 1, indicating that the incident light energy is completely conserved. Under this condition, Eq. (2.b) and Eq. (3.b) become functions of the reflectivity R and phase retardation δ, as illustrated in Fig. 3(a) and Fig. 3(b).

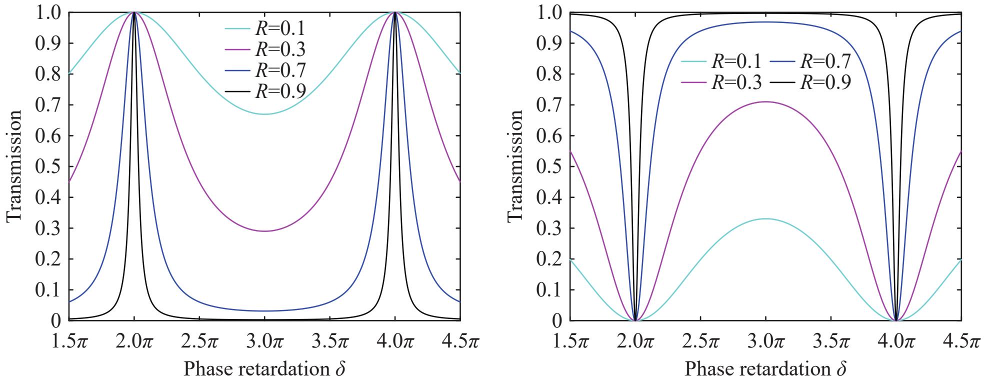

Fig. 3 (a) Transmitted radiation of a F-P cavity; (b) Reflected radiation of a F-P cavity

In the case of transmission, when the phase retardation δ is an integer multiple of 2π, the transmitted light intensity reaches a maximum, resulting in bright fringes. Conversely, when δ is a half-integer multiple of 2π, the intensity is minimized, producing dark fringes.

$$n=\delta(2\pi)^{-1}=2\mu d\sigma\cos\theta \quad , \tag{8}$$

where n is the interference order. Specifically, when n is an integer, bright interference fringes appear; when n is a half-integer, dark fringes are observed. At high reflectivity (R), the interference pattern of the transmitted light consists of fine bright fringes against a dark background, as shown in Fig. 4(b). In contrast, the reflected light displays narrow dark fringes on a bright background, as shown in Fig. 4(a). Consequently, reflected interference fringes are less distinguishable and are therefore rarely used.

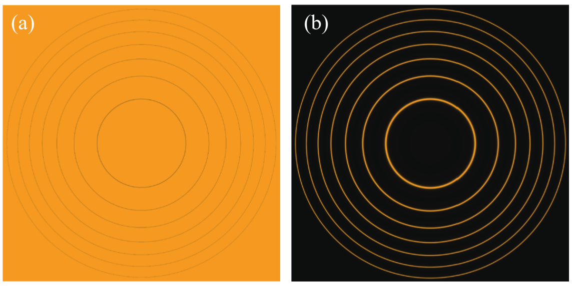

Fig. 4 (a) Interference pattern of reflected light and (b)Interference pattern of transmitted light (light source: sodium lamp)

The central interference order of the transmitted radiation, i.e., the interference that occurs normal to the surface of the etalon, is defined as:

$$n_0 = 2\mu d\sigma \quad , \tag{9}$$

2.1.1 Free spectral range

In a typical experimental setup, the optical axis of the lens is aligned perpendicular to the F–P cavity, resulting in a series of concentric circular interference fringes, as illustrated in Fig. 5 and Fig. 6. When two light beams with wavenumbers σ_1 and σ_2 ($\sigma_1 > \sigma_2$) enter the F-P cavity, an increase in the difference between the two wavenumbers leads to an increasing separation between the radii of interference rings of the same order. As a result, the m-th order fringe of σ_2 may overlap with the (m+1)-th order fringe of σ_1, causing ambiguity between different orders of interference rings and preventing effective spectral separation[23]. To address this issue, the F-P cavity, as a spectral separation element, has a maximum allowable wavelength interval, defined as the free spectral range (FSR), as shown in Fig. 7.

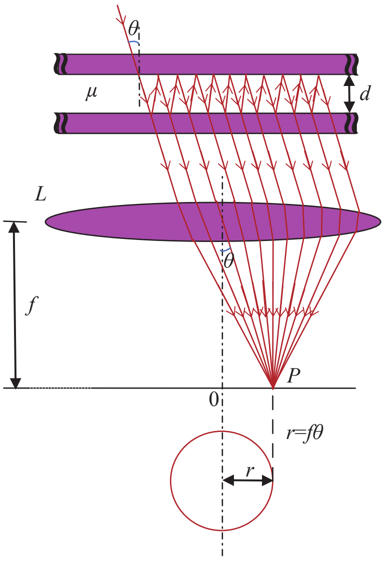

Fig. 5 Experimental setup for multi-beam interference.

The free spectral range expressed in terms of wavenumber is given by:

$$\Delta\sigma = \sigma_1 - \sigma_2 = \frac{1}{2\mu d} \quad , \tag{10}$$

Based on the relation σ=1/λ between wavenumber and wavelength, the FSR in terms of wavelength can be written as:

$$\Delta\lambda = \lambda_2 - \lambda_1 = \frac{\lambda_1\lambda_2}{2\mu d} \quad , \tag{11}$$

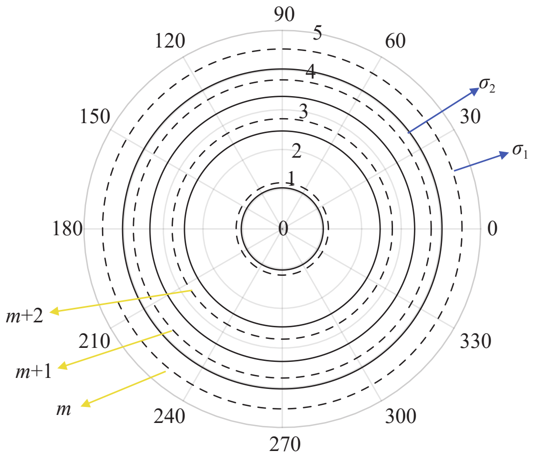

Fig. 6 Two sets of interfering circles in the F-P cavity. $m+i$ (i = 0, 1, 2) are the interference order.

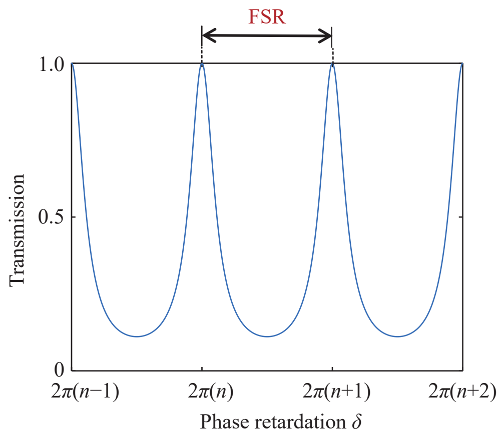

Fig. 7 Diagram illustrating the Free Spectral Range (FSR)

2.1.2 Half-width at Half-height

According to the transmitted intensity distribution curve shown in Fig. 3, the width of the interference fringes is finite and primarily determined by the reflectivity R in Eq. (3.b). The spectral linewidth at half the maximum transmitted intensity is defined as the half-width at half-height (HWHH), denoted as a, as illustrated in Fig. 8. Based on Eq. (3.d) with A=0, we can calculate the half-width at half-height:

$$a = 2\sin^{-1}\left[(1-R)\left(2R^{\frac{1}{2}}\right)^{-1}\right] \quad , \tag{12}$$

When R approaches 1, Eq. (7.a) can be approximated by:

$$a \approx (1-R)R^{-1/2} \quad , \qquad (13)$$

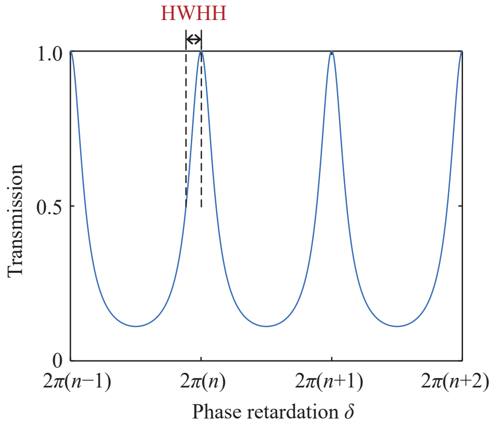

Fig. 8 Diagram of half-width at half-height (HWHH)

The above definition of HWHH assumes a spectral period of 2π for the F–P cavity. To generalize the analysis and allow for scaling, the normalized HWHH is described as:

$$a^{*} = a(2\pi)^{-1} = \pi^{-1}\sin^{-1}\left[(1-R)\left(2R^{1/2}\right)^{-1}\right] \quad , \qquad (14)$$

The inverse of the normalized HWHH is referred to as the reflective finesse of the F-P cavity, denoted by N_R:

$$N_R = (2a^{*})^{-1} = \pi\left\{2sin^{-1}\left[(1-R)\left(2R^{1/2}\right)^{-1}\right]\right\}^{-1} \quad , \qquad (15)$$

$$N_R \approx \pi R^{1/2}(1-R)^{-1} \quad , \qquad (16)$$

Eq. (8) and Eq. (9) indicate that both the normalized HWHH and the reflective finesse N_R depend solely on the reflectivity R, and are intrinsic properties of the F–P cavity.

2.2 Finite-size aperture

The above conclusions are based on the assumption that the mirrors of the F–P cavity have infinite physical dimensions and thus allow an infinite number of light reflections. However, in practical applications, the mirrors are of finite size. In imaging systems, where many off-axis rays are involved, larger mirror apertures are required to maintain interference conditions.

In this study, a model of an F-P cavity with finite aperture size is established[24]. The entrance aperture has a diameter of $2a$, the exit aperture is $2A$, and the light is incident at angle θ. It undergoes multiple reflections and transmissions within the F-P cavity, producing multibeam interference, as shown in Fig. 9.

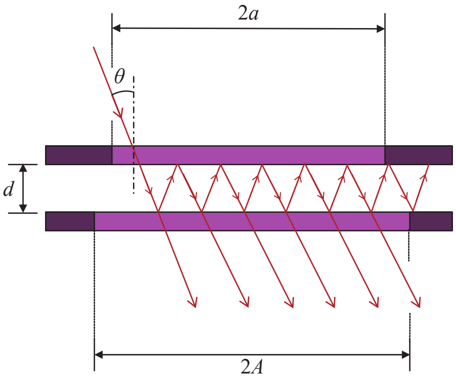

Fig. 9 Schematic diagram of F-P cavity with finite aperture

We classify these reflections into two categories: (1) reflections occurring within the entrance aperture; (2) reflections occurring within the exit aperture but outside the entrance aperture. As shown in the schematic, the number of internal reflections is finite and can be quantified. For light incident at angle θ in an F–P cavity with gap spacing d, the lateral displacement per reflection is:

$$l = 2d\tan\theta \quad , \qquad (17)$$

Therefore, the number of reflections within the entrance aperture is:

$$k = \frac{2a}{l} = \frac{2a}{2d\tan\theta} \approx \frac{a}{d\theta} \quad , \qquad (18)$$

where k is the integer closest to the maximum number of reflections occurring within the entrance aperture. The number of reflections occurring between the entrance and exit apertures (but outside the entrance aperture) is:

$$n = \frac{A-a}{2d\tan\theta} \approx \frac{A-a}{2d\theta} \quad , \qquad (19)$$

where n is the integer closest to the maximum number of reflections in that region.

For an F–P cavity with finite aperture, the transmitted intensity becomes:

$$Y_{n,k}(\delta) = Y_t(\delta)\{1 + R^{2n+2}(1 - R^{2k})[k(1 - R^2)]^{-1} - 2Y_{t_{A=0}}(\delta)R^{n+1}[k(1 - R)^2]^{-1} \times [\cos[(n+1)\delta] - R\cos(n\delta) - R^k\cos[(n+k+1)\delta] + R^{k+1}\cos[(n+k)\delta]]\} \quad , \tag{20}$$

where $Y_t(\delta)$ is the transmitted intensity function of the ideal F-P cavity with absorption/scattering (Eq. (3.b)), $Y_{t,A=0}(\delta)$ is the intensity function without absorption/scattering (also derived from Eq. (3.b)). Eq. (13) applies to both the equal-aperture case (n=0) and the larger-exit-aperture case (n>0). In most practical applications, F–P cavities are designed with equal entrance and exit apertures. Under this condition, Eq. (13) simplifies to:

$$Y_k(\delta) = Y_t(\delta)\{1 + R^2(1 - R^{2k})[k(1 - R^2)]^{-1} - 2RY_{t,A=O}(\delta)[k(1 - R)^2]^{-1} \times [\cos\delta - R - R^k cos[(k+1)\delta] + R^{k+1}\cos(k\delta)]\} \quad , \tag{21}$$

2.3 Surface defect error

After machining, the reflection surfaces of the F-P cavity are not perfectly flat, which inevitably affects its optical performance. In most studies, an F-P cavity with surface defects is modeled as a collection of elemental F-P cavities, each with slightly different gap spacings. The transmission intensity of such a cavity is expressed as the weighted sum of the transmission intensities of these elemental cavities, using an appropriate distribution function.

The first type of surface defects is microscopic inhomogeneity, characterized by small-scale surface roughness and randomly distributed imperfections. However, the root-mean-square (RMS) variation of this distribution is typically negligible compared to the aperture size and cavity spacing. For such defects, the gap distribution is commonly modeled by a Gaussian (normal) distribution per unit area[25]. In this case, the transmission intensity of the F–P cavity is given by:

$$Y(\delta_0) = \tau^2\left(\pi^{1/2}\Delta\delta\right)^{-1} \times \left\{\int_{-\infty}^{\infty} \exp - \left[(\delta_i - \delta_0)^2\Delta\delta^{-2}\right]\left[1 + R^2 - 2R\cos\delta_i\right]^{-1} d\delta_i\right\} = \left[1 - A(1-R)^{-1}\right]^2(1-R)(1+R)^{-1} \times \left[1 + 2\sum_{k=1}^{k=\infty} R^k \exp - \left(2^{-1}\Delta\delta k\right)^2 \cos(k\delta_0)\right] \quad , \tag{22}$$

Here, $\Delta\delta$ denotes the phase dispersion caused by variations in the microscopic cavity spacing, which is related to the spectral width of the light source.

The second type of defect is surface curvature[26], for which the gap distribution is assumed to be uniform over a specific phase interval. Consequently, the corresponding wavenumber distribution is constant within a narrow range and zero outside this range. The following discussion considers circular flats. The transmission intensity of an F-P cavity with curvature defects is expressed as:

$$Y(\sigma_0) = \left[1 - A(1-R)^{-1}\right]^2(1-R)(1+R)^{-1} \times \left\{1 + 2\sum_{k=1}^{k=\infty} R^k sinc\left(2kdf^* \cos\left(2\pi\sigma_0\Delta\sigma^{-1} cos\theta\right)\right)\right\} \quad , \tag{23}$$

where $\mathrm{sin}c(x) = (\pi x)^{-1}\sin(\pi x)$.

2.4 Performance Indicator

2.4.1 Spectral resolution

Because the width of the interference fringes is finite, the resolving power of the F-P cavity- that is, its ability to distinguish two closely spaced spectral lines of equal intensity-is inherently limited. While various definitions of spectral resolving power exist, they typically yield similar results. The most widely accepted definition for the F–P cavity is based on the Houston criterion, which states that two bright interference fringes of equal intensity and different wavelengths are considered resolvable when their centers are separated by at least the full width at half maximum (FWHM) of the fringe. Therefore, if the HWHH and the normalized HWHH are denoted by

a and a^*, respectively, the spectral resolving power of the F-P cavity is given by:

$$R=\sigma(2a)^{-1}=n_0(2a^*)^{-1}=n_0N_R \quad , \qquad (24)$$

Here, σ is the average wavenumber of the two spectral lines, n_0 is the central interference order, and N_R is the reflective finesse. From the above, the limit of the F–P cavity's resolving capability (i.e., the minimum resolvable spectral interval) is

$$r=\frac{\sigma}{R}=2a=2a^*\Delta\sigma=\Delta\sigma N_R^{-1} \quad , \qquad (25)$$

Therefore, the spectral resolution of the F-P cavity is determined by its full width at half height (FWHH), denoted as $2a$, as shown in Fig. 10.

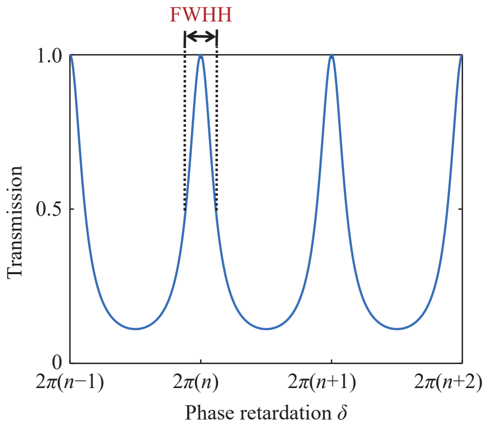

Fig. 10　Diagram of the full width at half height (FWHH)

2.4.2　Contrast

In the case where A=0, Eq. (3) indicates that the transmission at the peak of the interference fringe reaches 1, while the minimum transmission value is $(1-R)^2(1+R)^{-2}$. Based on this, the contrast C is defined as:

$$C=Y_t(\delta)_{max}[Y_t(\delta)_{min}]^{-1}=\frac{1}{(1-R)^2(1+R)^{-2}}=(1+R)^2(1-R)^{-2} \quad , \qquad (26)$$

Contrast C serve as a measure of the ability of the F-P cavity to distinguish between strong and weak spectral lines within the same spectrum. As illustrated in Fig. 11, there are two transmitted spectral lines, where the intensity of the weaker line is only 1/100 of that of the stronger one. The ability to resolve such differences improves as the reflectance R increases.

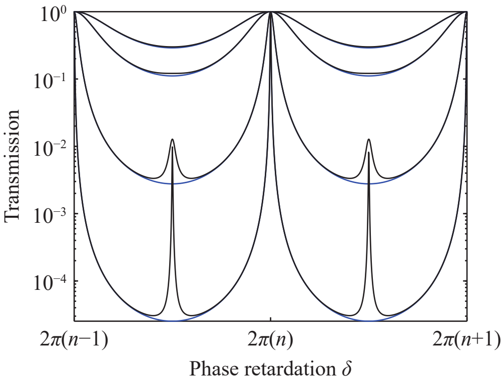

Fig. 11　Effect of contrast on the transmission spectrum

3　Physical modeling of F-P cavities

3.1　Initial model construction

In this paper, methane (CH_4) is selected as the target gas, and the parameters of the Fabry–Perot (F–P) cavity are designed to match its absorption spectrum. According to the absorption line intensity data for methane in the short-wave infrared (SWIR) region obtained from the HITRAN database, as shown in Fig. 12, the spectral region with the strongest absorption lines-5 970 cm^{-1} to 6 135 cm^{-1} (corresponding to 1 630–1 675 nm)-is chosen as the target band. Previous studies have shown that the methane Q-branch exhibits strong absorption in this spectral range[27].

To scan the corresponding spectral band, the interference rings must move relative to the scanning aperture. This relative movement can be achieved using Eq. (4), which indicates that to vary the wavenumber σ, one must adjust one of the following parameters on the right-hand side: the refractive index μ of the gap medium, the gap spacing d, or the incidence angle θ. The scanned spectra across different wavenumbers within the target range are illustrated in Fig. 13.

The method of changing the refractive index μ of the inter-mirror medium is called refractive index scanning method; Adjusting the mirror spacing

d is known as mechanical scanning. Modifying the angle of incidence θ corresponds to spatial scanning. In this paper, spatial scanning is adopted. As the F–P cavity uses a natural light source, the incident light inherently contains a range of angles, eliminating the need for mechanical movement to vary θ. This approach simplifies the mechanical design and enhances system stability.

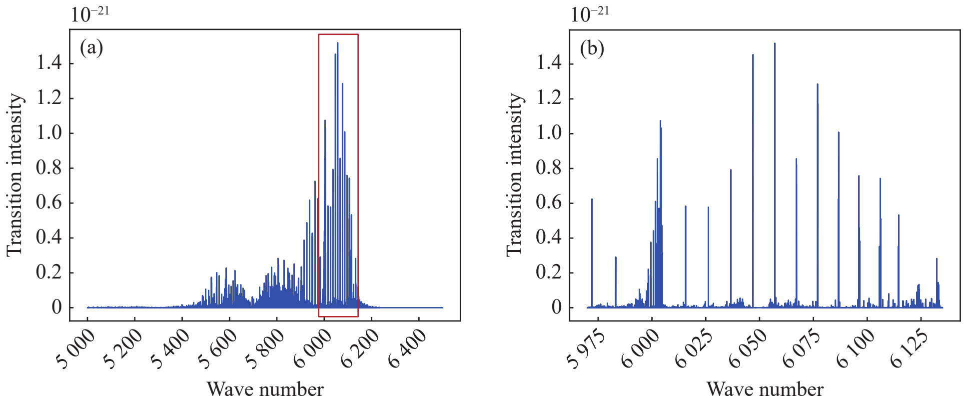

Fig. 12 (a) Transition intensity of methane in the SWIR band; (b) Transition intensity of methane in the 1 630-1675nm range.

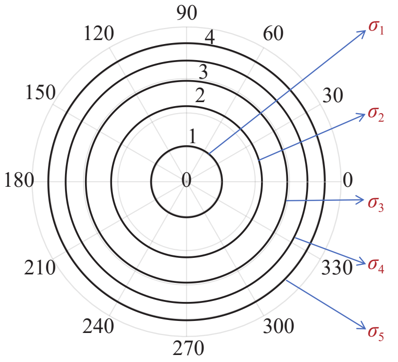

Fig. 13 Schematic of fringe movement relative to the scanning aperture

To ensure that the entire spectrum within the imaging field of view is covered, the free spectral range (FSR) must be selected such that at least three transmission peaks appear within the spectral bandpass for a given angle of incidence θ[28], as shown in Fig. 14.

The target bandwidth is 45 nm, so the FSR should be no more than 15 nm. Given that the F–P cavity operates in air ($\mu \approx 1$), and using the FSR equation (Eq. 6), the cavity gap d is chosen as 92 000 nm, resulting in an FSR of $\Delta\lambda$ = 14.838 3 nm.

To enable accurate column density monitoring of methane, the required spectral resolution of the satellite-based imaging spectrometer is within 0.3 nm. Considering potential line-broadening effects, we conservatively target a spectral resolution of 0.1 nm under ideal conditions. The F-P cavity's spectral resolution is governed by the full-width at half-maximum (FWHM) of its transmission curve:

$$r = 2a = \frac{\Delta\lambda}{N_R^{-1}} = \frac{\Delta\lambda}{\dfrac{\pi\sqrt{R}}{1-R}} \quad , \qquad (27)$$

From this equation, the FWHH depends on the reflectance R once the FSR is determined. Setting R = 0.98 yields a finesse N_R=155.5 and a FWHM of 0.095 nm.

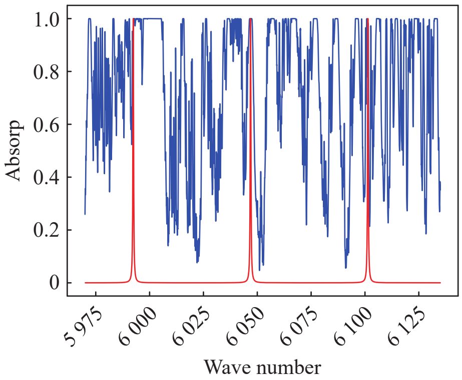

Fig. 14 Absorption spectrum of methane. Blue: Methane absorption spectrum from HITRAN (1 630–1 675 nm,); Red: F-P cavity transmission peaks.

Constructive transmission through the F–P cavity occurs when the phase difference between adjacent rays is an integer multiple of 2π, i.e.,

$$\delta = 4\pi\mu d\sigma\cos\theta = \frac{4\pi\mu d\cos\theta}{\lambda} = 2m\pi \quad , \qquad (28)$$

$$2\mu d\cos\theta = m\lambda \quad , \qquad (29)$$

where m is the interference order (an integer). The relationship among wavelength λ, incidence angle θ and interference order m is shown in Fig. 15.

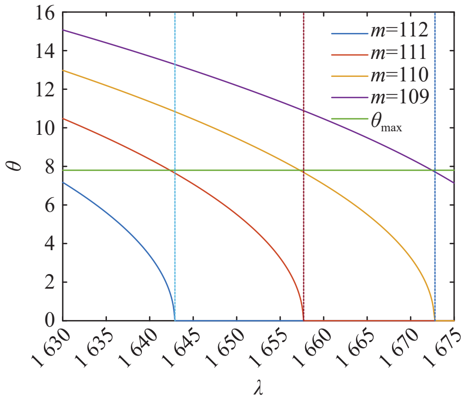

Fig. 15　Relationship among incidence angle, wavelength and interference order

Based on this relationship and the selected FSR, an incidence angle range of 0 to ±7.8° is chosen. Since the F-P cavity accommodates continuous incident angles, continuous wavelengths within the target spectral band can be sampled.

Ultimately, the spectrogram appears as a set of interference rings, as shown in Fig. 4 and Fig. 13. In the imaging system, the radius of these rings is approximately proportional to the angle of incidence. Thus, instead of dispersing light by wavelength, the system filters specific wavelengths based on their radial position. As the observed light has passed through the atmosphere, dark rings of specific radii correspond to molecular absorption lines.

Each interference order of the F–P cavity repeats periodically, with adjacent orders spaced by the FSR. Based on Eq. (3), the transmitted intensity distribution within a single FSR is illustrated in Fig. 16. As seen, the interference rings become denser toward the center of the pattern, indicating reduced angular dispersion. Fig. 17 further analyzes the angular dispersion across the target spectral range. It shows that angular dispersion varies from 0.004 to 0.05 rad/nm, exhibiting both high spectral uniformity and periodicity consistent with Fig. 15.

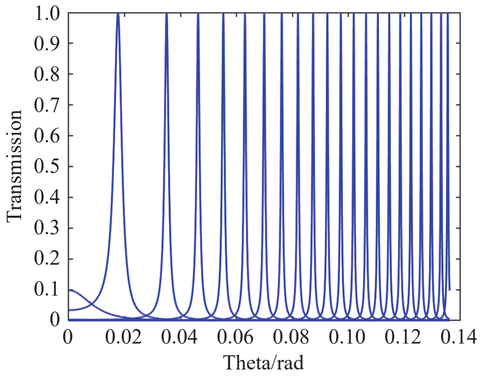

Fig. 16　Transmitted intensity distribution within a single FSR

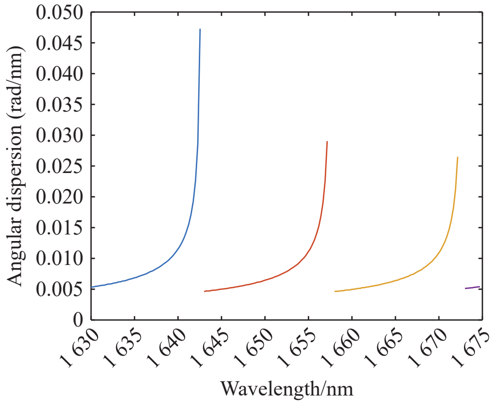

Fig. 17　Angular dispersion across the entire target spectral range

3.2　Physical model optimization

3.2.1　Finite-size aperture

Depending on the intended application of the F-P cavity, there exists a minimum aperture diameter of the mirror surface that ensures the interference pattern produced by a finite-size F-P cavity closely resembles that of the ideal case. Based on the mathematical model of an F-P cavity with finite aperture size, the transmission characteristics are illustrated in Fig. 18.

As shown in Fig. 18, with a decrease in the number of reflections k, the transmission loss of the F-P cavity increases progressively. Consequently, the transmission peak decreases, the profile broadens, and the contrast of the interference fringes diminishes. This leads to a broadening of the spectral lines, ultimately resulting in a reduction of the spectral resolving power of the F-P cavity.

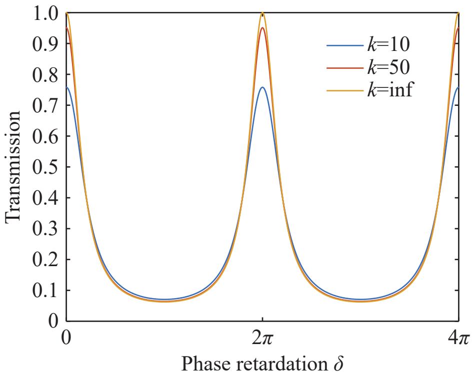

Fig. 18 Transmission for a finite-size matched-aperture F-P cavity

When the absorption coefficient A=0 and k is sufficiently large, Eq. (14) can be approximated as:

$$Y_k(\delta) \cong Y_t(\delta)\{1+[k(1-R^2)]^{-1}\times [R^2-2RY_t(\delta)(1+R)(1-R)^{-1}\times(\cos\delta-R)]\} \quad , \tag{30}$$

With further simplifying, the equation becomes:

$$Y_k(\delta) \cong Y_t(\delta)[1+[k(1-R^2)^{-1}]]-(1+R)[k(1-R)]^{-1}Y_t^{2}(\delta) \quad , \tag{31}$$

There are two terms in the above equation that are inversely proportional to k, one of which is also proportional to the square of the ideal F-P cavity function. Therefore, as k increases, the performance of the finite-size F-P cavity approaches that of the ideal one.

According to Eq. (14), the relationships between the peak transmission $Y_k(0)$, contrast C_k, full-width at half-height FWHH and the number of reflections k can be derived. These relationships, representing the influence of cavity size on spectral performance, are shown in Fig. 19.

For ease of analysis, we represent the spectral width as a/a_k, where a is the FWHH of the ideal F-P cavity, and a_k is the FWHH of the finite-size cavity, derived from Eq. (23). As seen in Fig. 19, increasing k leads to a larger aperture, higher peak transmission, greater contrast, and narrower FWHM. This translates to improved spectral resolution, making the performance of the finite-size F-P cavity increasingly similar to the ideal case and resulting in clearer interference patterns.

However, in practice, the cavity size cannot be infinitely large. As light undergoes more reflections, its energy decays exponentially, and rays reflected multiple times contribute little to the overall interference pattern. Moreover, increasing the size of the F-P cavity significantly raises manufacturing costs. For these reasons, we examine the performance enhancement relative to cavity size, as shown in Fig. 20.

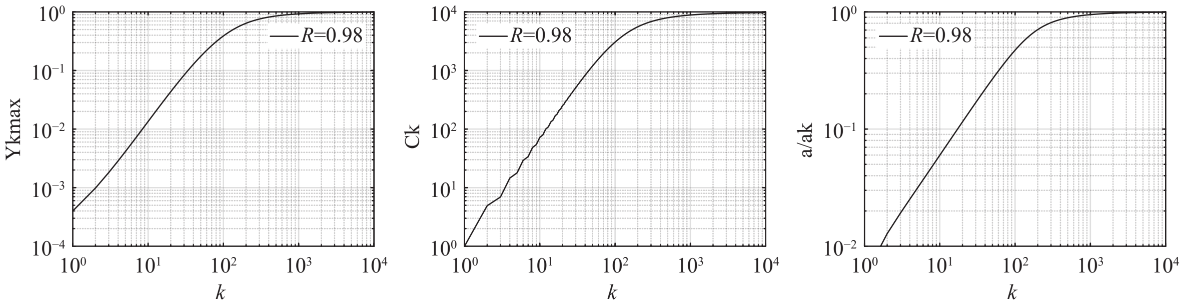

Fig. 19 Maximum transmission, contrast and FWHH as a function of the effective cavity size k

From Fig. 20, it is evident that when the number of reflections approaches 1,000, the slopes of the curves for transmission, contrast, and FWHM all tend toward zero. Beyond this point, further increases in k yield negligible improvements in cavity performance.

Thus, to determine an optimal number of reflections, we focus our analysis on the range k=300–

600. The reflection number corresponding to each peak transmission value is used to calculate the associated FWHM and aperture size via Eq. (11), Eq. (14) and Eq. (23), as shown in Table 2.

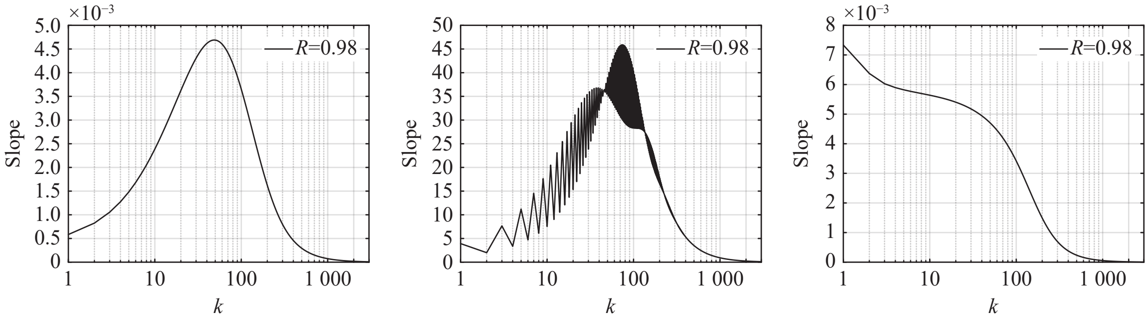

Fig. 20 Slope of peak transmission $Y_k(0)$, contrast C_k and FWHH as functions of effective cavity size k

Tab. 2 Performance parameters of F-P cavity for varying number of reflections

Maximum transmission $Y_k(0)$	Number of reflections k	Aperture size $2a$/mm	Width of profile FWHH/nm
0.88	615	15.5	0.1044
0.87	568	14.3	0.1053
0.86	527	13.3	0.1063
0.85	492	12.4	0.1072
0.84	461	11.6	0.1081
0.83	434	11.0	0.1091
0.82	410	10.4	0.1105
0.81	389	9.8	0.1115
0.80	369	9.6	0.1124
0.79	352	9.3	0.1134
0.78	336	8.9	0.1148
0.77	321	8.5	0.1157
0.76	308	8.1	0.1171

Based on these results, we select k=380 and an aperture size of $2a$=9.6 mm. According to optical design requirements, the minimum aperture needed to fully receive the incident beam is 6.8 mm. Therefore, the total aperture radius is set to 13 mm. The corresponding performance parameters are listed in Table 3.

Tab. 3 Performance parameters of F-P cavity under chosen aperture size

$Y_k(0)$	k	$2a$/mm	$(2a+6.8/2)$/mm	FWHH/nm
0.806	380	9.6	13	0.1115

3.2.2 Wedge angle

In practice applications, the two parallel planes forming the F-P cavity consist of a combination of a physical substrate with a certain thickness and a mirror with a specific reflectivity. The total thickness of the mirror assembly varies depending on the actual design; in this case, it is 20 mm. However, the presence of finite mirror thickness introduces several undesirable effects-most notably, light undergoes reflection and refraction within the thickness of the mirror itself, thereby forming an unintended interference cavity that is independent of the primary interference region. The stray light generated from this spurious cavity can partially distort the desired interference pattern.

To suppress the influence of this extraneous cavity, two primary methods are commonly employed: (1) applying an anti-reflective coating to the backside of the mirror substrate to reduce its reflectivity, and (2) introducing a wedge angle on the backside of the mirror substrate. By combining both methods-i.e., applying an anti-reflective coating to a wedge-shaped backside-the impact of the spurious interference cavity on the final interference pattern can be reduced to a negligible level.

Therefore, in coordination with the overall optical system design, a wedge angle of 0.5° is introduced on the backside of both mirrors in the F-P cavity. Simultaneously, anti-reflective coatings are applied to these back surfaces to effectively eliminate the adverse effects caused by the finite thickness of the mirror substrates.

3.2.3 Gap spacing tolerance

The F-P cavity employed in this work adopts a fixed air gap structure, where the spacing between the two parallel planes is maintained by a cylindrical spacer. During the manufacturing and assembly processes, machining and measurement errors inevitably introduce deviations in the gap spacing. To ensure that the F-P cavity meets technical specifications, it is essential to control the air gap within a defined tolerance range.

The gap spacing d is a critical parameter that influences key characteristics of the F-P cavity, such as the free spectral range, spectral resolution, interference order, and number of reflections. According to Eq. (22), any variation in gap spacing necessitates a corresponding adjustment in the interference order for the target spectral band, in order to ensure effective spectral coverage across the entire target range. Table 4 presents the relationship among the incidence angle, wavelength, and interference order for different gap spacings. In each subfigure of the table, the number displayed beneath the figure indicates the corresponding air-gap size (in nanometers) used to generate the curve.

As the gap spacing increases, the interference order within the target spectral band also increases. Among all the gap spacings considered, only at a spacing of 89,000 nm does the incident light fail to cover the entire target band, resulting in partial spectral loss near the wavelength of 1 663.7 nm, as illustrated in Fig. 21.

According to Eq. (6), the free spectral range (FSR) of the F-P cavity is inversely proportional to the gap spacing d. To adequately sample the spectrum across the imaging field of view, it is desirable to have three transmission peaks at each angle of incidence. If the FSR is too small, some incidence angles may produce fewer than three peaks; if the FSR is too large, more than three peaks may occur.

By analyzing the plots in Table 4, we draw the following conclusions: (1) When the gap spacing is less than 92,000 nm, the FSR increases. At a spacing of 90,000 nm, the range of incidence angles producing only two transmission peaks accounts for 3.4% of the total incidence angle range; at 91,000 nm, this proportion reduces to 1.1%. (2) When the gap spacing exceeds 92,000 nm, the FSR decreases. At gap spacings up to 97,000 nm, the incidence angles producing more than three transmission peaks account for up to 12% of the full range. However, once the spacing exceeds 97,000 nm, this proportion increases to more than 15%. Therefore, we initially selected a gap-spacing range of [91 000, 97 000] nm for further analysis.

Additionally, increasing the air gap spacing leads to larger optical path differences per reflection and a reduction in the number of effective reflections k, resulting in broader in full-width at half-height (FWHH) values and lower spectral resolution. Under ideal conditions, we calculated the theoretical FWHM for each gap spacing in the selected range, as well as the actual number of reflections and FWHM values under finite aperture conditions, as shown in Table 5.

From the data in Table 5, it can be seen that variations in gap spacing have a greater impact on the FWHM of the spectral line profile than the corresponding changes in the number of reflections under finite aperture conditions. Specifically, when the gap spacing is greater than 92000nm, the actual FWHM decreases slightly, resulting in a modest improvement in spectral resolution. Conversely, when the spacing is below 92000nm, the FWHM increases slightly, leading to a marginal reduction in resolution.

However, even in the worst-case scenarios, the increase in FWHM remains under 0.3nm, which is within the acceptable range for our system. Therefore, we selected the gap-spacing interval of [91 000, 97 000] nm as it meets the technical requirements of the F-P cavity design.

Tab. 4 Relationship among incident angle, wavelength and interference order for different gap spacings

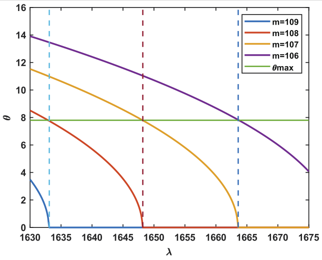 89 000	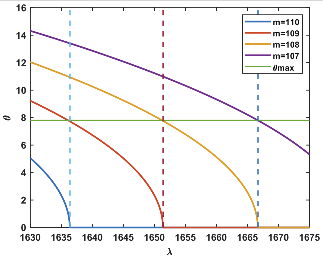 90 000	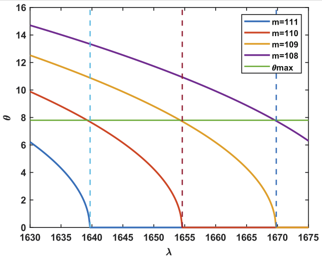 91 000
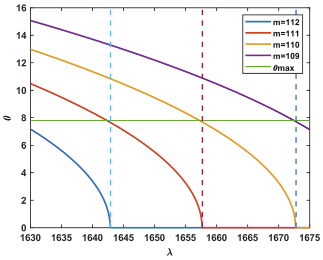 92 000	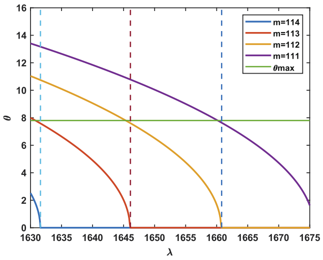 93 000	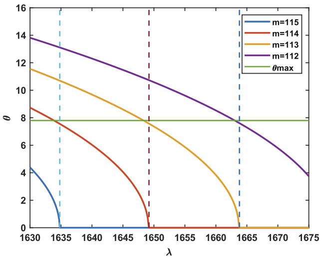 94 000
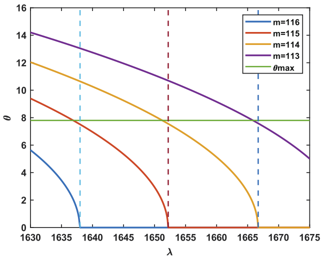 95 000	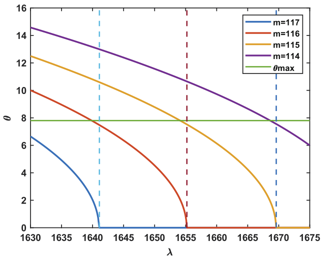 96 000	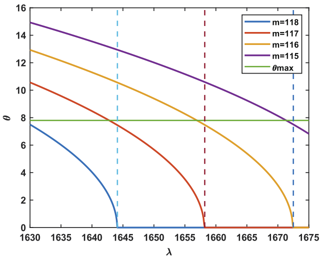 97 000
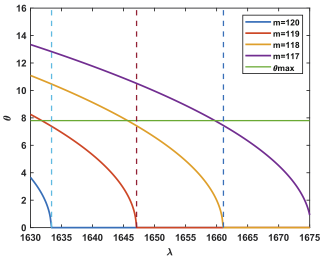 98 000	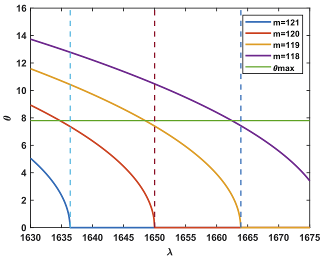 99 000	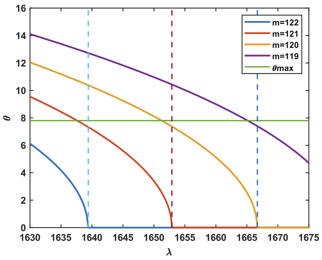 100 000

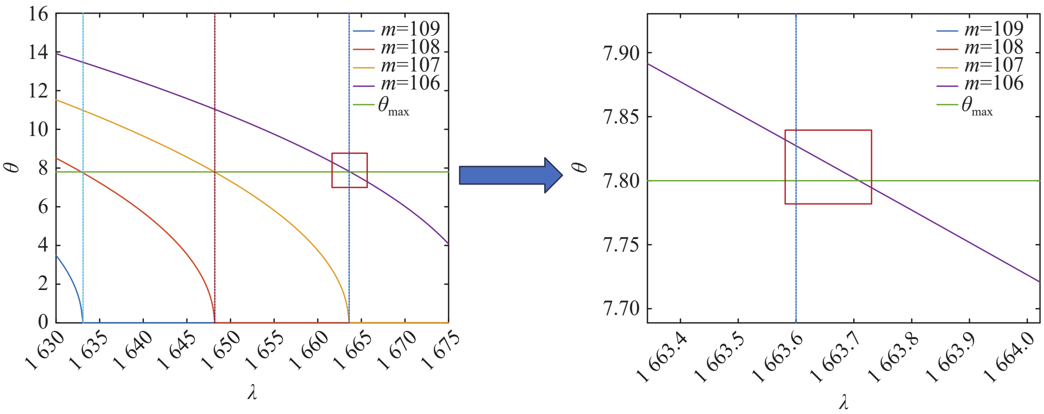

Fig. 21 Curves of incident angle, wavelength and interference order for a gap spacing of 89 000 nm

Tab. 5 Parameters of the F-P cavity for each gap spacing

Gap spacing/nm	91 000	92 000	93 000	94 000	95 000	96 000	97 000
Ideal FWHH/nm	0.0965	0.0954	0.0944	0.0934	0.0924	0.0915	0.0905
number of reflections *k*	384	380	375	371	368	364	360
Actual FWHH/nm	0.1121	0.1115	0.1090	0.1085	0.1079	0.1074	0.1069

3.2.4 Surface defect error

The dispersion caused by microscopic random inhomogeneity defects is related to variations in the wavenumber of the incident light. By associating the frequency variation of the light source with the gap spacing variation of the F-P cavity, and expressing this variation in terms of wavelength, the equivalent half-width at half-height (HWHH) of the defect distribution, expressed as a fraction of the wavelength (λ/m), can be written as:

$$df = 2.35\Delta\sigma m^{-1} \quad , \qquad (32)$$

The corresponding normalized half-width at half-height is:

$$df^{*} = 2.35m^{-1} \quad , \qquad (33)$$

From Eq. (25) and Eq. (26), the microscopic random inhomogeneity defect distribution is independent of both the gap spacing and the reflectivity of the F-P cavity. Therefore, the half-width at half-height of the microscopic random inhomogeneity defect distribution remains a constant for a given F-P cavity. Referring to the reflection finesse, the surface finesse N_D associated with such defects can be expressed as:

$$N_D = (2df^{*})^{-1} = (4.71)^{-1}m \quad , \qquad (34)$$

By substituting *df** into the exponential term of Eq. (15) and converting it into phase terms, we obtain:

$$\left(2^{-1}\Delta\delta\right)^2 = (\pi df^{*})^2[\ln(2)]^{-1} \quad ,$$

When curvature defects are small relative to the F-P cavity's gap spacing and planar surface area, the equivalent HWHH of the resulting defect distribution can also be expressed in terms of the wavelength fraction (λ/m) as:

$$df = \Delta\sigma m^{-1} \quad , \qquad (35)$$

The normalized form becomes:

$$df^{*} = m^{-1} \quad , \qquad (36)$$

Accordingly, the surface finesse is:

$$N_D = (2df^{*})^{-1} = 2^{-1}m \quad , \qquad (37)$$

Since both the normalized HWHH a^{*} and the defect-induced HWHH *df** are independent of the F-P cavity's gap spacing and reflectivity, the overall profile width e^{*} for a cavity with surface defects is also constant for a given instrument. The finesse of the F-P cavity with surface defects is then defined as

$$N_e = (2e^{*})^{-1} = (2a^{*} \oplus df^{*})^{-1} \quad , \qquad (38)$$

where $\oplus$ denotes the cumulative effect on the profile width. However, the actual HWHH of the F-P cavity must be calculated using Eq. (15) or Eq. (16).

Using Eq. (15) and Eq. (16), we evaluated the impact of two types of surface defects-microscopic random inhomogeneity and curvature-on the F-P cavity, as illustrated in Fig. 22 and Fig. 23.

As shown in Fig. 22 and Fig. 23, with increasing *m*, surface finesse improves, surface defects diminish, transmission peaks increase, contrast enhances, and the integrated profile width decreases. This leads to improved spectral resolution of the F-P cavity. Therefore, a larger *m* value corresponds to better spectral performance.

The primary factor influencing the impact of surface defects on F-P cavity performance is surface finesse, which in turn depends on the type of defect. In the following section, we further analyze the parameters used to evaluate mirror surface quality based on defect type.

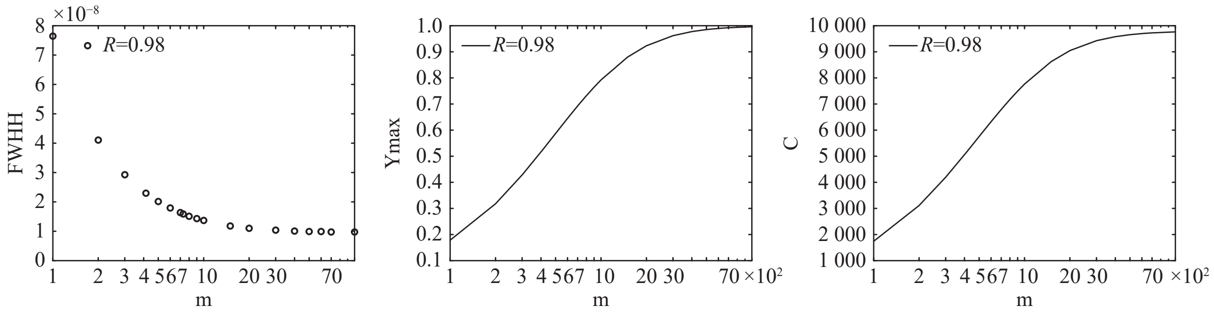

Fig. 22 Effect of microscopic random inhomogeneity defects on FWHH, peak transmission and contrast

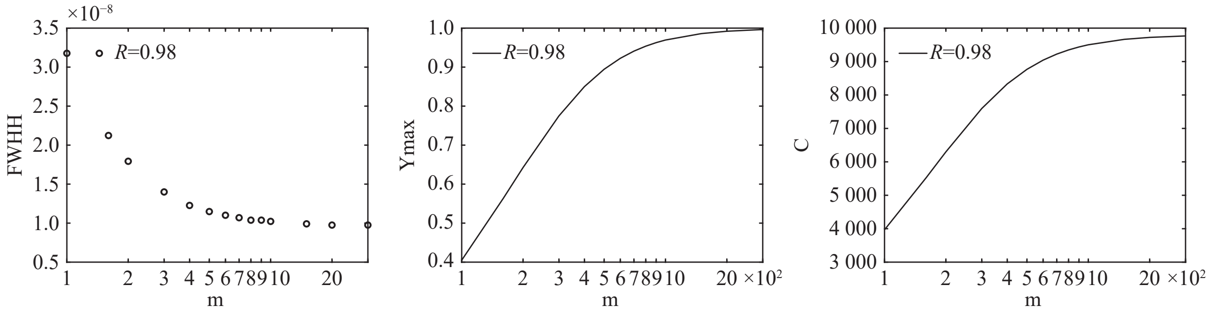

Fig. 23 Effect of curvature defects on FWHH, peak transmission and contrast

3.2.4.1 Surface roughness

Surface roughness is classified as a micro-geometric surface error, primarily influenced by microscopic random inhomogeneity defects, typically exhibiting a Gaussian distribution. In this context, surface roughness is described by R_z, defined as λ/m_G.

Considering the influence of microscopic random inhomogeneity defects on the F-P cavity as illustrated in Fig. 22, and taking into account the fabrication limits of optical lenses, the value of m_G is set to 414. Consequently, the surface roughness R_z is $\lambda/414$ (approximately 4 nm).

The surface finesse N_{DG} of the F-P cavity, when dominated by microscopic random inhomogeneity defects, is given by:

$$N_{DG} = (4.71)^{-1} m_G \quad ,$$

Substituting m_G = 414, the F-P cavity yields surface finesse of 87.9, a peak transmission of 0.53, a contrast of 5 165, and a FWHH of 0.23 nm.

3.2.4.2 Surface precision

Surface figure accuracy is primarily impacted by curvature-related errors. Here, the peak-to-valley (PV) deviation is adopted as the metric for evaluating surface figure quality, represented by λ/m_c.

Based on the effect of curvature defects on F-P cavity shown in Fig. 23, and considering the machining limitations of optical components, the value of m_C is chosen as 160, resulting in a PV deviation of $\lambda/160$.

The surface finesse N_{DC} under curvature defect dominance is expressed as:

$$N_{DC} = 2^{-1} m_C \quad ,$$

With m_C=160, the F-P cavity exhibits a finesse of 80, a peak transmission of 0.56, a contrast of 5 524, and a FWHH of 0.21 nm.

3.2.4.3 Parallelism

In equal-inclination interference scenarios of the F-P cavity, the achievable parallelism between two plates is determined by the width of interference fringes. Hence, the lower limit of parallelism is defined by the cavity's finesse. Given that the finesse is influenced by both curvature defects and random micro-inhomogeneity, the effective finesse is:

$$N_e = (2e^*)^{-1} = (2a^* \oplus df_G{}^* \oplus df_C{}^*)^{-1} \quad , \qquad (39)$$

The required parallelism between the F-P cavity plates is $\lambda/(4N_e)$. The instrumental function of the cavity is given by:

$$Y(\sigma_0)=\left[1-A(1-R)^{-1}\right]^2(1-R)(1+R)^{-1}\times\left\{1+2\sum_{k=1}^{k=\infty}R^k\exp-\left(2^{-1}\Delta\delta k\right)^2\mathrm{sinc}\,(2kdf_C{}^*)\cos\left(2\pi k\sigma_0\Delta\sigma^{-1}\cos\theta\right)\right\}=$$

$$\left[1-A(1-R)^{-1}\right]^2(1-R)(1+R)^{-1}\times\left\{1+2\sum_{k=1}^{k=\infty}R^k\exp-\left(\frac{2.35k\pi}{m_G\sqrt{\ln 2}}\right)^2\frac{\sin\left(\dfrac{2k\pi}{m_C}\right)}{\dfrac{2k\pi}{m_C}}\cos\left(2\pi k\sigma_0\Delta\sigma^{-1}\cos\theta\right)\right\}\quad,\qquad（40）$$

Neglecting the absorption losses and substituting m_G=414, m_C=160 into Eq. (32) we obtain the HWHH(e) as 0.14 nm. Additionally:

$$e^*=\frac{e}{\Delta\lambda}=0.009$$
$$N_e=(2e^*)^{-1}=53.6\quad,$$

Therefore, the required parallelism between the two plates is λ/214.4.

3.3 Performance analysis

By combining Eq. (14) and Eq. (32), we evaluate the performance of the F-P cavity designed as a spectroscopic element for methane point-source emission monitoring. The spectral resolution achieved is 0.29 nm, with a peak transmission of 0.43, which satisfies the functional requirements for methane detection, as illustrated in Fig. 24. In addition, the contrast ratio reaches 3934, which is approximately 40% of that of an ideal F-P cavity, and the system exhibits high spectral uniformity, with angular dispersion ranging from 0.001 to 0.015 rad/cm^{-1} within the target spectral band, as shown in Fig. 25.

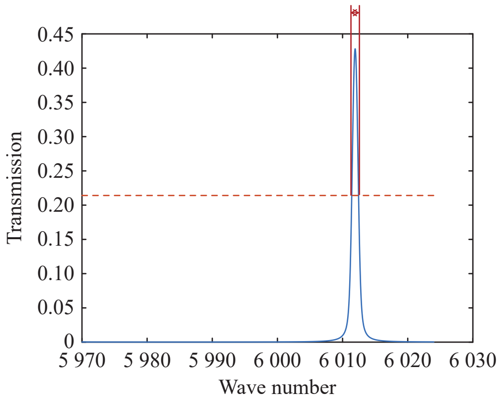

Fig. 24 Performance diagram of the F-P cavity as a spectroscopic element

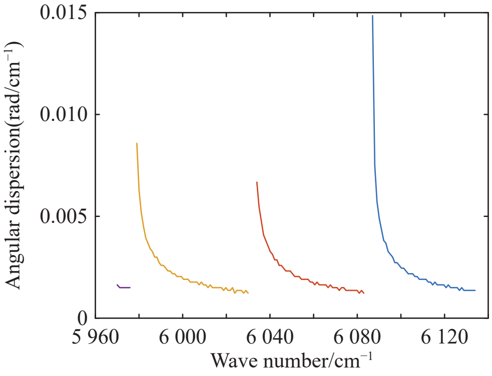

Fig. 25 Angular dispersion of the F-P cavity across the entire target spectral range

4 Conclusion

This thesis focuses on the application of the F-P cavity in industrial-grade point-source methane emission monitoring, and conducts a systematic study on theoretical modeling and design optimization. First, an initial theoretical model of the F-P cavity is developed based on multi-beam interference theory, and then finite aperture effects and surface defects are incorporated to refine the model, laying the foundation for subsequent research. Secondly, regarding physical model development, key parameters of the F-P cavity are designed and optimized based on the methane absorption spectrum and system monitoring requirements, including aperture diameter, wedge angle, gap tolerance, and reflective surface quality. Finally, the optimized F-P cavity achieves a spectral resolution of 0.29 nm, fully meeting the technical specifications for methane emission monitoring.

References:

[1] 张岑, 李伟. 欧美甲烷减排战略与油气行业减排行动分析[J]. 国际石油经济, 2021, 29(12): 16-23.
ZHANG C, LI W. Analysis of methane emission reduction strategies in Europe and America and actions of oil and gas industry[J]. *International Petroleum Economics*, 2021, 29(12): 16-23. (in Chinese).

[2] 陈迎, 巢清尘.《碳达峰、碳中和 100 问》[J]. 国企管理, 2021(16): 12.
CHEN Y, CHAO Q CH. 100 Questions on carbon peak and carbon neutrality[J]. *China State-Owned Enterprise Management*, 2021(16): 12. (in Chinese) **(查阅网上资料, 未找到本条文献英文信息, 请确认)**.

[3] 秦凯, 何秦, 康涵书, 等. 煤炭行业甲烷排放卫星遥感研究进展与展望[J]. 光学学报, 2023, 43(18): 1899908.
QIN K, HE Q, KANG H SH, *et al*.. Progress and prospect of satellite remote sensing research applied to methane emissions from the coal industry[J]. *Acta Optica Sinica*, 2023, 43(18): 1899908. (in Chinese).

[4] VEEFKIND J P, ABEN I, MCMULLAN K, *et al*.. TROPOMI on the ESA Sentinel-5 precursor: a GMES mission for global observations of the atmospheric composition for climate, air quality and ozone layer applications[J]. *Remote Sensing of Environment*, 2012, 120: 70-83.

[5] GLUMB R, DAVIS G, LIETZKE C. The TANSO-FTS-2 instrument for the GOSAT-2 greenhouse gas monitoring mission[C]. *Proceedings of IGARSS 2014 - 2014 IEEE International Geoscience and Remote Sensing Symposium*, IEEE, 2014: 1238-1240.

[6] 熊伟. "高分五号"卫星大气主要温室气体监测仪 (特邀)[J]. 红外与激光工程, 2019, 48(3): 303002.
XIONG W. Greenhouse gases Monitoring Instrument (GMI) on GF-5 satellite (invited)[J]. *Infrared and Laser Engineering*, 2019, 48(3): 303002. (in Chinese).

[7] JERVIS D, MCKEEVER J, DURAK B O A, *et al*.. The GHGSat-D imaging spectrometer[J]. *Atmospheric Measurement Techniques*, 2021, 14(3): 2127-2140.

[8] PIGNATTI S, PALOMBO A, PASCUCCI S, *et al*. . The PRISMA hyperspectral mission: science activities and opportunities for agriculture and land monitoring[C]. *Proceedings of 2013 IEEE International Geoscience and Remote Sensing Symposium*, IEEE, 2013: 4558-4561.

[9] STUFFLER T, KAUFMANN C, HOFER S, *et al*.. The EnMAP hyperspectral imager—an advanced optical payload for future applications in Earth observation programmes[J]. *Acta Astronautica*, 2007, 61(1-6): 115-120.

[10] 刘银年, 孙德新, 胡晓宁, 等. 高分五号可见短波红外高光谱相机设计与研制[J]. 遥感学报, 2020, 24(4): 333-344.
LIU Y N, SUN D X, HU X N, *et al*.. Development of visible and short-wave infrared hyperspectral imager onboard GF-5 satellite[J]. *Journal of Remote Sensing (Chinese)*, 2020, 24(4): 333-344. (in Chinese).

[11] 刘银年, 孙德新, 韩波, 等. 资源一号 02D 卫星可见短波红外高光谱相机研制[J]. 航天器工程, 2020, 29(6): 85-92.
LIU Y N, SUN D X, HAN B, *et al*.. Development of advanced visible and short-wave infrared hyperspectral imager onboard ZY-1-02D satellite[J]. *Spacecraft Engineering*, 2020, 29(6): 85-92. (in Chinese).

[12] ZHU B Q, ZHANG K Y, ZHANG W P. Optomechanical preparation of photon number-squeezed states with a pair of thermal reservoirs of opposite temperatures[J]. *Photonics Research*, 2023, 11(9): A26.

[13] GEORGIEVA E M, HEAPS W S. Robust IR remote sensing technique of the total column of trace gases including carbon dioxide and methane[C]. *Proceedings of Geoscience and Remote Sensing Symposium*, IEEE, 2011: 997-1000.

[14] VARGAS-RODRÍGUEZ E, RUTT H N. Design of CO, CO_2 and CH_4 gas sensors based on correlation spectroscopy using a Fabry–Perot interferometer[J]. *Sensors and Actuators B: Chemical*, 2009, 137(2): 410-419.

[15] YE J S. High finesse Fabry–Perot filter for the measurement of methane gas by using multiline absorption spectroscopy[J]. *Optical Engineering*, 2014, 53(2): 024103.

[16] LIANG T T, QIAO SH D, CHEN Y J, *et al*.. High-sensitivity methane detection based on QEPAS and H-QEPAS technologies combined with a self-designed 8.7 kHz quartz tuning fork[J]. *Photoacoustics*, 2024, 36: 100592.

[17] QIAO SH D, HE Y, SUN H Y, *et al*. . Ultra-highly sensitive dual gases detection based on photoacoustic spectroscopy by exploiting a long-wave, high-power, wide-tunable, single-longitudinal-mode solid-state laser[J]. *Light*: *Science & Applications*, 2024, 13(1): 100.

[18] FUCHS C, KUHN J, BOBROWSKI N, *et al*.. Quantitative imaging of volcanic SO_2 plumes using Fabry–Pérot interferometer correlation spectroscopy[J]. *Atmospheric Measurement Techniques*, 2021, 14(1): 295-307.

[19] LV Y SH, XIE P H, XU J, *et al*.. Methane measurement method based on F-P angle-dependent correlation

spectroscopy[J]. *Optics Express*, 2024, 32(13): 23646-23662.

[20] VARON D J, JACOB D J, JERVIS D, *et al*.. Quantifying time-averaged methane emissions from individual coal mine vents with GHGSat-D satellite observations[J]. *Environmental Science & Technology*, 2020, 54(16): 10246-10253.

[21] 王建宇, 李春来. 高光谱遥感信息获取[M]. 武汉: 湖北科学技术出版社, 2021.
WANG J Y, LI CH L. *Hyperspectral Remote Sensing Data Acquisition*[M]. Wuhan: Hubei Science and Technology Press, 2021. (in Chinese).

[22] MCKEEVER J, JERVIS D, STRUPLER M. Microsatellites spot mystery methane leaks[J]. *IEEE Spectrum*, 2020, 57(11): 38-43.

[23] 石顺祥, 王学恩, 刘劲松. 物理光学与应用光学[M]. 西安: 西安电子科技大学出版社, 2000.
SHI SH X, WANG X E, LIU J S. *Physical Optics and Applied Optics*[M]. Xi'an: Xidian University Press, 2000. (in Chinese) **(查阅网上资料, 未找到本条文献英文信息, 请确认)**.

[24] SLUIS K L V, MCNALLY J R. Fabry-Perot interferometer with finite apertures[J]. *Journal of the Optical Society of America*, 1956, 46(1): 39-46.

[25] HERNANDEZ G. *Fabry-Perot Interferometers*[M]. Cambridge: Cambridge University Press, 1986.

[26] ROESLER F L. 12. Fabry-Perot Instruments for astronomy[J]. *Methods in Experimental Physics*, 1974, 12: 531-569.

[27] 张宇, 王一丁, 李黎, 等. 甲烷红外吸收光谱原理与处理技术分析[J]. 光谱学与光谱分析, 2008, 28(11): 2515-2519.
ZHANG Y, WANG Y D, LI L, *et al*.. The principle and technical analysis of methane detection using infrared absorption spectroscopy[J]. *Spectroscopy and Spectral Analysis*, 2008, 28(11): 2515-2519. (in Chinese).

[28] JERVIS D, MCKEEVER J, DURAK B O A, *et al*.. The GHGSat-D imaging spectrometer[J]. *Atmospheric Measurement Techniques*, 2021, 14(3): 2127-2140. **(查阅网上资料, 本条文献与第 7 条文献重复, 请确认)**.

Author Biographies:

LU Chuang (1999—), Master, Changchun Institute of Optics, Fine Mechanics and Physics, Chinese Academy of Sciences. Her research interests are on interferometric ultra-fine spectral spatial detection and imaging technology. E-mail: luchuang22@mails.ucas.ac.cn.

LI Zong-xuan (1986—), Professor, Changchun Institute of Optics, Fine Mechanics and Physics, Chinese Academy of Sciences. His research interests are on overall technology for space optics payload optical machines and integrated analysis and optimization of optical machine dynamics. E-mail: lizongxuan@ciomp.ac.cn